JOURNAL OF AIRCRAFT
Vol. 46, No. 3, May–June 2009

Self-Adaptive Upwinding for Large Eddy Simulation of Turbulent Flows on Unstructured Elements

Nima Tajallipour,* Babak Babaee Owlam,† and Marius Paraschivoiu‡
Concordia University, Montreal, Quebec H3G 1M8, Canada

DOI: 10.2514/1.38945

A self-adaptive upwinding method for large eddy simulation is proposed to reduce the numerical dissipation of a low-order numerical scheme on unstructured elements. This method is used to extend an existing Reynolds-averaged Navier–Stokes code to a large eddy simulation code by adjusting the contribution of the upwinding term to the convective flux. This adjustment is essentially controlled by the intensity of the local wiggle and reduces the upwind contribution in the Roe-MUSCL scheme. First, the stability characteristic of the new scheme is studied using a channel flow stability test. It is essential to ensure that the proposed scheme is able to adjust upwinding in the presence of very high gradients and that it prohibits the divergence of the simulation. Second, the decaying isotropic turbulence is simulated to study the capability of the new scheme to generate the suitable decaying rate for the total kinetic energy and its influence over the slope of the energy spectrum at different computational times. Finally, the flow separation phenomenon over a NACA0025 profile is numerically investigated and results are compared with experimental data.

Nomenclature

a_∞ = average ambient speed of sound
C_{noise} = coefficient of noise
C_S = Smagorinsky constant
$E(k)$ = energy spectrum
$E(t)$ = total kinetic energy
$E_{11}(k)$ = one-dimensional energy spectrum
$\tilde{e}$ = filtered total energy per unit mass
$\bar{f}(x,t)$ = filtered function
$\tilde{f}(x,t)$ = Favre-filtered function
$f''(x,t)$ = fluctuating component of the filtered function
$G(x,\Delta)$ = filter function
L = reference length scale
M_t = turbulence Mach number
Pr = Prandtl number
Pr_t = turbulent Prandtl number
$\bar{p}$ = mean pressure
Q_j = subgrid-scale heat flux
$\hat{q}$ = average value of q evaluated at the boundary of a cell
q_-, q_+ = internodal values between the nodes of an edge
Re_C = chord Reynolds number
$\tilde{S}_{ij}$ = rate-of-strain tensor
$\tilde{T}$ = Favre-filtered static temperature
T_∞ = reference static temperature
U_∞ = reference velocity
$\tilde{u}_i$ = cartesian components of the filtered velocity
$\mathbf{X}_i$ = position vector of node i
x_i = Cartesian coordinates ($i = 1, 2, 3$)
α = angle of attack
β = parameters used to calculate the internodal values in the MUSCL scheme
γ = parameters to adjust the upwinding in the MUSCL scheme
Δ = filtering size
Δx^+ = streamwise size of the elements in wall units
Δy^+ = size of the elements normal to the solid walls in wall units
Δz^+ = spanwise size of elements in wall units
θ = intensity of the local wiggle
$\mu(\tilde{T})$ = molecular viscosity
$\bar{\rho}$ = mean density
ρ_∞ = reference density
$\tilde{\sigma}_{ij}$ = molecular viscous stress tensor
τ_{ij} = subgrid-scale stress tensor

I. Introduction

THE importance of applying accurate numerical methods in large eddy simulation (LES), especially when it involves an upwinding term in the flux calculation, has been previously reported in the literature [1–3]. The upwind schemes, regardless of the applied numerical method, add some artificial dissipation and are therefore known to be much more stable than central-difference schemes and are used successfully for Reynolds-averaged Navier–Stokes (RANS) simulations. This additional dissipation, however, can negatively influence the accuracy. Spyropoulos and Blaisdell [1] used a fifth-order upwind-biased finite difference scheme for the inviscid flux calculation to simulate the turbulent flow inside a channel. They recognized the fact that the upwinding schemes provide artificial dissipation; therefore, they preferred to use the upwind-biased scheme. Mary and Sagaut [2] used a second-order MUSCL, cell-centered, control volume scheme to simulate the flow around an airfoil using structured multiblock meshes. They applied a sensor to minimize the numerical dissipation originated from its upwinding. Andersson et al. [3] simulated a compressible jet using a third-order upwinding scheme in which the contribution of the upwinding term was decreased to one-eighth to make the numerical method less dissipative.

The additional dissipation of a numerical method highly depends on the nature of emulated flow and the local resolution of the grid, and under some circumstances, it can even be higher than the dissipation of the applied subgrid-scale model. That is specially the

---

Presented as Paper 674 at the 46th AIAA Aerospace Sciences Meeting and Exhibit, Reno, NV, 7 January–10 February 2008; received 4 June 2008; revision received 23 January 2009; accepted for publication 31 January 2009.

*Research Assistant, Department of Mechanical and Industrial Engineering, 1455 de Maisonneuve Boulevard West, Room EV 14-115; n_tajall@encs.concordia.ca.

†Research Assistant, Department of Mechanical and Industrial Engineering, 1455 de Maisonneuve Boulevard West, Room EV 14-115; bbabaee@gmail.com.

‡Associate Professor, Department of Mechanical and Industrial Engineering, 1455 de Maisonneuve Boulevard West, Room EV 4-149; paraschi@encs.concordia.ca.

case when a low-order numerical discretization is used, such as that applied in this paper. For example, Hahn and Drikakis [4] simulated decaying turbulence and compressible flow around open cavities for low- and high-order Reynolds numbers. They concluded that the numerical dissipation of their numerical method was satisfactory; therefore, the addition of an explicit subgrid model (SGS) was not justifiable.

In this paper, we use the second-order Roe-MUSCL flux calculation ($\beta\gamma$ scheme) for the LES, and the objective is to evaluate and possibly control the effects of its numerical dissipative error. In MUSCL ($\beta\gamma$ scheme), the contribution of the upwinding term is adjusted using coefficient γ, which is directly multiplied into that term during the flux calculation. Coefficient β is also used to predict the value of variables at the boundaries of control volume cells.

A complete analysis of the accuracy of MUSCL ($\beta\gamma$ scheme) and its relation to the structure of the generated grid has been reported by Carpentier [5]. In that study, the dissipative and dispersive error terms of 2-D advection equation have been analyzed using two different meshes (a uniformly distributed triangular mesh and a structured quadrangular mesh). He concluded that $\beta = 1/3$ and $\gamma = 0.0$ will result in a fourth-order dispersive error and a fifth-order dissipative error. This high-order dissipative error requires the scheme to have no upwinding ($\gamma = 0.0$). It was also observed that these error terms were functions of the Courant–Friedrichs–Lewy (CFL) number related to the applied fourth-order Runge-Kutta time discretization scheme. If $\beta = 1/3$ but $\gamma \neq 0.0$, then the dissipative error will be of third order, whereas the dispersive error will remain of fourth order. In addition, it was also found that the uniform triangular mesh potentially has higher dispersive and dissipative error in comparison with quadrangular mesh.

As a result, there have been several attempts to lower the applied value of γ and consequently decrease the numerical dissipation of the MUSCL method. For example, Bui [6] simulated the turbulent flow inside a square duct using Roe-MUSCL ($\beta\gamma$ scheme) and a structured grid. He tried to use the smallest possible value for γ for which the simulation was still stable. Camarri and Salvetti [7] applied a second-order mixed finite-volume/finite-element code using MUSCL to study the contribution of upwinding to the numerical dissipation and its interaction with SGS. They also used the lowest possible fraction of the upwinding term to minimize the dissipative error and to satisfy the stability condition of the simulation. In all of these cases, several simulations had to be carried out to determine the lowest value of γ that was still able to keep the simulation stable.

Ciardi et al. [8] recently developed a new scheme for the unstructured meshes based on finite volumes for inviscid and viscous flux calculations. They adjusted the contribution of the upwinding term using a wiggle detector, and there was therefore no need for several simulations to determine the lowest value of γ. In their method, the objective was to completely damp the wiggles of a certain size detected by the sensor. This method, however, can partially lead to damping of the energy in the smallest scales captured in the simulation. Because the smallest scales of simulation fall within the inertial subrange in LES, it is necessary to preserve the energy of such scales [9].

In this paper, a new self-adaptive upwinding method inspired by [8,10] is developed and implemented. It is compatible with classic numerical schemes of compressible flows based on Roe-MUSCL ($\beta\gamma$ scheme) and is also applicable to unstructured girds. It uses a wiggle detector that has been inspired by [11]. The wiggle detector proposed by [8] detects the wiggles along three consecutive edges that are not necessarily collinear and it could lead to some uncertainty. Therefore, a new method for wiggle detection is proposed here that is expected to be more reliable. In addition, the developed scheme does not completely damp the wiggles detected by the wiggle detector, but instead permits some wiggles to develop up to a preset threshold of intensity inside the computational domain. The importance of that is shown to be crucial when adjusting the slope of the energy spectrum.

It is generally agreed that turbulent flows are characterized by their unsteadiness and unpredictability, and the largest part of the turbulent energy is constructed by truly random motions that could be the remains of old coherent structures [9]. We also know that in a typical simulation, whenever the grid resolution is not high enough to capture all the scales of the flow (LES), the application of a central scheme would generate random fluctuations and wiggles. That is the case when γ is lowered by the wiggle detector. As a result, the developed scheme introduces a degree of randomness into the solution that could be favorable and generate more realistic results.

In this paper, the stability characteristic of the new scheme is first studied using a channel flow stability test. It is essential to ensure that the proposed scheme is able to adjust upwinding in the presence of very high gradients and prohibits the divergence of the simulation. Second, the decaying isotropic turbulence is simulated to study the capability of the new scheme to generate the suitable decaying rate for the total kinetic energy and its influence over the slope of the energy spectrum at different computational times. Finally, the separation of flow over a NACA0025 wing is simulated to further examine the new scheme in a numerically more difficult situation. In the following sections of this paper, the governing equations are introduced, followed by the description of the numerical methodology, then the three numerical tests are presented, and the results are compared with experimental data.

II. Governing Equations

The governing equations are the spatially filtered compressible Navier–Stokes equations. The spatial filtering separates the small-scale eddies of the flow and accumulates their effects in the SGS stresses and heat transfer terms. The remaining large energy-containing eddies generated by the large-scale turbulent motions and the dynamic motions inside the flowfield are simulated.

For an arbitrary function, $\bar{f}(x_i, t)$ is defined as

$$\bar{f}(x_i, t) = \int_D G(x_i - \xi_i, \Delta) f(\xi_i, t) \mathrm{d}\xi_i \tag{1}$$

where Δ is the filtering size and is related to the size of the computational mesh. For compressible flows, the Favre-filtering operation is defined as

$$\tilde{f}(x_i, t) = \frac{\overline{\rho f}}{\bar{\rho}} \tag{2}$$

By this definition, a variable is decomposed into its Favre-filtered component and fluctuating component according to

$$f(x_i, t) = \tilde{f}(x_i, t) + f''(x_i, t) \tag{3}$$

If we assume that the filtering operations commute with the derivative operators and then apply the definitions in Eqs. (1) and (2) to the compressible Navier–Stokes equations, the filtered governing equations are obtained as follows [12–15]:

$$\frac{\partial \bar{\rho}}{\partial t} + \frac{\partial \bar{\rho} \tilde{u}_i}{\partial x_i} = 0 \tag{4}$$

$$\frac{\partial \bar{\rho} \tilde{u}_i}{\partial t} + \frac{\partial \bar{\rho} \tilde{u}_i \tilde{u}_j}{\partial x_j} = -\frac{\partial \bar{p}}{\partial x_i} + \frac{\partial (\tau_{ij} + \tilde{\sigma}_{ij})}{\partial x_j} \tag{5}$$

$$\frac{\partial \bar{\rho} \tilde{e}}{\partial t} + \frac{\partial (\bar{\rho} \tilde{e} + \bar{p}) \tilde{u}_j}{\partial x_j} = \frac{\partial \left(Q_j + (\mu(\tilde{T}) C_p / Pr)(\partial \tilde{T} / \partial x_j) + (\tau_{ij} + \tilde{\sigma}_{ij}) \tilde{u}_i \right)}{\partial x_j} \tag{6}$$

$$\bar{p} = \bar{\rho} R \tilde{T} \tag{7}$$

where $Pr = 0.715$, and $\tilde{e}$ is the filtered total energy per unit mass and is defined as

$$\bar\rho\,\tilde e = \bar\rho c_v \tilde T + \tfrac{1}{2}\bar\rho \tilde u_i \tilde u_i \tag{8}$$

The molecular viscous stress tensor $\tilde\sigma_{ij}$ is approximated by

$$\tilde\sigma_{ij} = \mu(\tilde T)\left(-\frac{2}{3}\frac{\partial \tilde u_k}{\partial x_k}\delta_{ij} + \frac{\partial \tilde u_i}{\partial x_j} + \frac{\partial \tilde u_j}{\partial x_i}\right) \tag{9}$$

where $\mu(\tilde T)$ is molecular viscosity and is calculated by the Sutherland equation:

$$\mu(\tilde T) = (1.711 \times 10^{-5})\left(\frac{\tilde T}{273.15}\right)^{2/3}\left(\frac{383.55}{\tilde T + 110.4}\right) \tag{10}$$

The subgrid-scale stress tensor τ_{ij} is modeled by compressible extension of the Smagorinsky subgrid scale as follows:

$$\tau_{ij} = -(\overline{\rho u_i u_j} - \bar\rho \tilde u_i \tilde u_j) = \bar\rho C_S \Delta^2 \sqrt{\tilde S_{kl}\tilde S_{kl}}(2\tilde S_{ij} - \tfrac{2}{3}\tilde S_{kk}\delta_{ij}) \tag{11}$$

The rate-of-strain tensor is defined as

$$\tilde S_{ij} = \frac{1}{2}\left(\frac{\partial \tilde u_i}{\partial x_j} + \frac{\partial \tilde u_j}{\partial x_i}\right) \tag{12}$$

and the model for the filtering size is

$$\Delta = (\mathrm{vol}(C_i))^{1/3} \tag{13}$$

where $\mathrm{vol}(C_i)$ is the volume of cell C_i, which belongs to node i. The subgrid-scale heat flux Q_j is modeled using the eddy viscosity model:

$$Q_j = -c_p(\overline{\rho u_j T} - \bar\rho \tilde u_j \tilde T) = \bar\rho c_P \frac{C_S}{Pr_t}\Delta^2 \sqrt{\tilde S_{kl}\tilde S_{kl}}\frac{\partial \tilde T}{\partial x_j} \tag{14}$$

where $Pr_t = 0.6$. We simplify the notation by dropping the tilde and overbar signs and also nondimensionalize the equations using the reference values ρ_∞, U_∞, $\rho_\infty U_\infty^2$, L, and T_∞. The governing equations take the following form:

$$\frac{\partial q}{\partial t} + \mathrm{div}(\mathbf{F}^{\mathrm{conv}} + \mathbf{F}^{\mathrm{diff}}) = 0 \tag{15}$$

$$q = \left\{\begin{matrix} \rho \\ \rho u_1 \\ \rho u_2 \\ \rho u_3 \\ \rho e \end{matrix}\right\} \tag{16}$$

$$F_j^{\mathrm{conv}} = \left\{\begin{matrix} \rho u_j \\ \rho u_j u_1 + p\delta_{j1} \\ \rho u_j u_2 + p\delta_{j2} \\ \rho u_j u_3 + p\delta_{j3} \\ u_j(\rho e + p) \end{matrix}\right\} \tag{17}$$

$$F_j^{\mathrm{diff}} = \left\{\begin{matrix} 0 \\ -\sigma_{j1} - \tau_{j1} \\ -\sigma_{j2} - \tau_{j2} \\ -\sigma_{j3} - \tau_{j3} \\ -\frac{\mu(\tilde T)C_p}{Pr}\frac{\partial \tilde T}{\partial x_j} - Q_j - u_k(\sigma_{kj} + \tau_{kj}) \end{matrix}\right\} \tag{18}$$

III. Numerical Method

The numerical method is a mixed finite-volume/finite-element method [13,16] that has been developed to solve the unsteady Navier–Stokes equations. It operates on unstructured grids using second-order MUSCL upwind formulation ($\beta\gamma$ scheme) for the convective fluxes and a second-order finite element method for the diffusive fluxes. As mentioned earlier, subgrid-scale terms are modeled by the Smagorinsky model. For the decaying isotropic turbulence, we assume $C_S = 0.01$, but for the flow separation over NACA0025, a much lower value ($C_S = 0.00014$) is used. During the channel flow simulation, the subgrid-scale model has been deactivated. A second-order implicit scheme is also used for the time discretization. The system of equations is then solved using an iterative generalized minimal residual solver.

The Roe-MUSCL method is the base for the convective flux calculation in this work. The normal component of the inviscid flux at the boundaries of neighboring cells is defined as the sum of an average term calculated by the fluxes of two nodes belonging to the edge that the flux is calculated along and an upwinding term:

$$\begin{aligned}\mathbf{F}^{\mathrm{conv}} \bullet \mathbf{n}_{ij} &= \tfrac{1}{2}(\mathbf{F}^{\mathrm{conv}}(q_+) + \mathbf{F}^{\mathrm{conv}}(q_-)) \\ &\quad \bullet \mathbf{n}_{ij} - \tfrac{1}{2}|\hat A(\hat q, \mathbf{n}_{ij})|(q_+ - q_-)\end{aligned} \tag{19}$$

where $\hat q$ is the average value of q evaluated at the boundary of a cell or control volume using the Roe method, and q_- and q_+ are calculated by interpolating the numerical flux of those two nodes to the boundaries of the cell ∂C_i (internodal values between nodes i and j):

$$q_- = q_i + \frac{1}{2}\left[(1-\beta)(q_j - q_i) + \beta(\nabla q)_{ij}^L \bullet \mathbf{n}_{ij}\right] \tag{20}$$

$$q_+ = q_j - \frac{1}{2}\left[(1-\beta)(q_j - q_i) + \beta(\nabla q)_{ji}^R \bullet \mathbf{n}_{ij}\right] \tag{21}$$

This approach is used to improve the precision of the method without changing the approximation space [13,16]. The parameter β determines to what extent central interpolation is used to calculate q_+ and q_-. As recommended in [5], we set the value of β equal to $1/3$ to minimize the dissipative and dispersive errors. Gradients $(\nabla q)_{ij}^L$ and $(\nabla q)_{ji}^R$ are defined as the left-hand and right-hand gradients (Figs. 1 and 2). These gradients are computed, respectively, on the upstream L and downstream R tetrahedrons associated with edge ij (Fig. 2). Local average gradients can also be used in Eqs. (20) and (21) as an approximation. This is an extension of the MUSCL method to the finite element, because the gradients of the variable vector (q) are computed using the finite element technique.

The Roe-MUSCL method has given good results for Euler or laminar simulations but it has been found to be too dissipative for LES [6,10]. To control the amount of Roe upwinding dissipation, a coefficient γ is used, such that

$$\begin{aligned}\mathbf{F}^{\mathrm{conv}} \bullet \mathbf{n}_{ij} &= \tfrac{1}{2}(\mathbf{F}^{\mathrm{conv}}(q_+) + \mathbf{F}^{\mathrm{conv}}(q_-)) \\ &\quad \bullet \mathbf{n}_{ij} - \gamma\{\tfrac{1}{2}|\hat A(\hat q, \mathbf{n}_{ij})|(q_+ - q_-)\}\end{aligned} \tag{22}$$

where γ can range between 0 and 1. In Eq. (22), $\gamma = 0$ corresponds to central differencing, and $\gamma = 1$ corresponds to the full MUSCL-Roe method. Omitting the Roe upwinding term altogether ($\gamma = 0$) causes all calculations to be unstable; therefore, for a given grid size, a minimum amount of upwinding dissipation is always required to provide stability. In general, a finer grid would require a smaller value of γ.

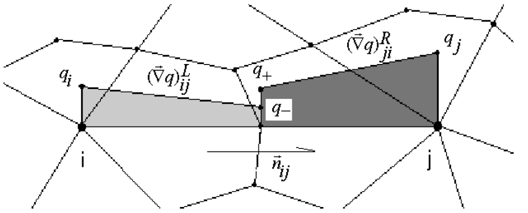

Fig. 1 Control volumes and convective flux calculation.

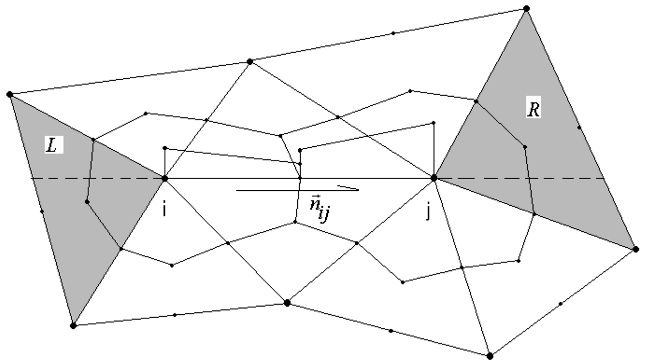

Fig. 2 Convective flux calculation.

To determine and adjust upwinding parameter γ dynamically, a wiggle detector has been implemented. It checks to see if the intensity of the local wiggle is higher than a preset value. If this is the case, then the scheme increases γ linearly toward the full MUSCL-Roe scheme. Otherwise, the scheme is more centered and γ is decreased.

In the present computations, we extend the wiggle definition given in [11] to our numerical method. A wiggle is assumed to be present along an arbitrary edge if the coefficient of direction changes twice along the edge in that direction. That is, if for any flow variable Φ ($\Phi \in [\rho, u, v, w, p]$)

$$(\Phi_i - \Phi_{i-1})(\Phi_{i+1} - \Phi_i) < 0 \tag{23}$$

$$(\Phi_{i+2} - \Phi_{i+1})(\Phi_{i+1} - \Phi_i) < 0 \tag{24}$$

are true, then a wiggle is present. A simplified example is illustrated in Fig. 3. In this example, there is a wiggle along the edge connecting nodes i and $i + 1$, but there is no wiggle along the edge connecting nodes $i - 1$ and i.

A new method is developed here to be a more general and appropriate approach for the purpose of LES. Consider a tetrahedron having ij as an edge (Fig. 2). Along ij, we compute $(\nabla\Phi)^C$ (C denotes centered):

$$(\nabla\Phi)^C \bullet \mathbf{n}_{ij} = (\Phi_j - \Phi_i)/|\mathbf{X}_j - \mathbf{X}_i|$$

where $\mathbf{X}_i$ and $\mathbf{X}_j$ are the position vectors of nodes i and j, respectively. We then replace inequalities (23) and (24) with the following:

$$\left[(\nabla\Phi)^L_{ij} \bullet \mathbf{n}_{ij}\right]\left[(\nabla\Phi)^C \bullet \mathbf{n}_{ij}\right] = \left[(\nabla\Phi)^L_{ij} \bullet \mathbf{n}_{ij}\right][(\Phi_j - \Phi_i)/|\mathbf{X}_j - \mathbf{X}_i|] < \theta \leq 0 \tag{25}$$

$$\left[(\nabla\Phi)^R_{ji} \bullet \mathbf{n}_{ij}\right]\left[(\nabla\Phi)^C \bullet \mathbf{n}_{ij}\right] = \left[(\nabla\Phi)^R_{ji} \bullet \mathbf{n}_{ij}\right][(\Phi_j - \Phi_i)/|\mathbf{X}_j - \mathbf{X}_i|] < \theta \leq 0 \tag{26}$$

If inequalities (25) and (26) are satisfied, then the intensity of the wiggle is more than the preset value θ, and γ should be increased. This increment is a linear function of

$$\theta - \min\{[(\nabla\Phi) \bullet \mathbf{n}_{ij}][(\nabla\Phi)^C \bullet \mathbf{n}_{ij}]\}$$

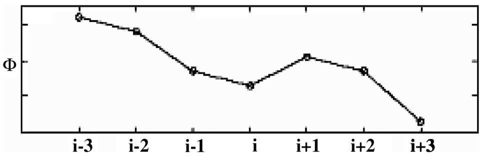

Fig. 3 Definition of a wiggle in the present computations [11].

On the other hand, when inequalities (25) and (26) are not satisfied, it implies that the intensity of the wiggle is less than the preset value θ, and γ can be decreased. This time, the decrement would be a linear function of

$$\max\{[(\nabla\Phi) \bullet \mathbf{n}_{ij}][(\nabla\Phi)^C \bullet \mathbf{n}_{ij}]\} - \theta$$

In both linear functions,

$$(\nabla\Phi) \in \left[(\nabla\Phi)^L_{ij}, (\nabla\Phi)^R_{ji}\right]$$

$\Phi \in [\rho, u, v, w, p]$, and the value of γ is chosen between 0 and 1. The value of θ is either negative or zero and usually has a small absolute value (≈ -0.00001 to -0.0001). The idea is to use the products of the gradients as a way to measure the intensity of a local wiggle.

For direct numerical simulation, the grid is fine enough to capture the smallest scales of eddies present in the flowfield. Therefore, the highest mode of energy spectrum $E(k)$ of the flow is lower than the highest mode that the numerical method can capture. In other words, the smallest eddies present in the flow have an average diameter that is fairly bigger than the local average size of the grid (h); therefore, no energy is expected to be present in the scales belonging to h. It implies that there should not be any local wiggle present in the flow, and θ in the nonequalities (25) and (26) must be set to zero. For LES, however, the situation is different, because even in the best cases, the cutoff mode is expected to fall within the inertial subrange; therefore, there will be some energy in the highest scales that are expected to be captured by the simulation. Therefore, θ is replaced by a negative and relatively small value that will represent the existence of energy in the smallest scales, and by changing the value of θ, the amount of that energy is adjusted.

IV. Numerical Results

At first, a channel flow simulation is carried out to test the stability of the scheme against the presence of strong gradients and fluctuations in the flow and also to measure its ability to adjust itself under such circumstances. Afterward, the decaying isotropic turbulence is simulated and the influence of the self-adaptive upwinding scheme over the total kinetic energy and the energy spectrum is studied. Its interaction with the external Smagorinsky SGS is also investigated. These test cases are validation and calibration steps for the development of the scheme. Finally, the scheme is used to simulate flow separation over a NACA0025 airfoil and the results are compared with the experimental data.

A. Channel Flow Simulation

In the channel flow test, the stability characteristics of the numerical method against strong gradients and fluctuations, artificially generated by a noise function in the flow initialization, is investigated. It is expected that the computed velocities result in a bounded total kinetic energy. If the scheme fails to satisfy this condition, it can be concluded with certainty that the numerical method is not suited to model turbulent flows. On the other hand, if it fulfills this condition, it does not automatically mean that it is a good model.

In this test, the flow through a channel presented in Fig. 4 is simulated. A similar test has been presented for an incompressible fluid simulation in [17] using hexahedral and tetrahedral elements. In the simulation presented here, only tetrahedral elements are used. The discretized domain contains 2302 tetrahedrons, 9658 nodes, and 2532 boundary faces. A rather coarse mesh is used in this simulation to reflect the typical situation in LES of turbulent flows in which there are too few degrees of freedom available for the simulated Reynolds number. The time step Δt of the simulation is set to 0.01, as is the case in [17]. At each time step, the residual is decreased 6 deg of magnitude to provide accurate results.

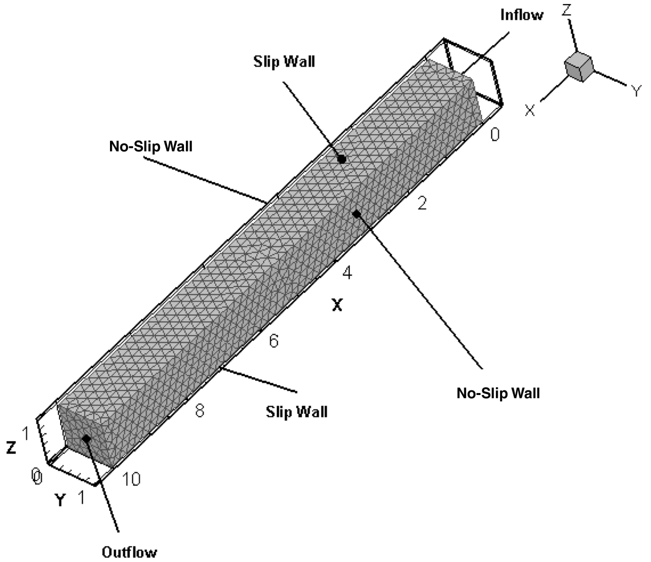

Fig. 4 Channel flow's grid and boundary conditions.

The inflow boundary condition is defined as

$$\mathbf{U}(t,0,y,z)=\begin{pmatrix}4y(1-y)\\0\\0\end{pmatrix} \tag{27}$$

On the lateral walls, a no-slip boundary condition is imposed, and on the top and bottom walls, a free-slip boundary condition is applied (Fig. 4). The flow leaves the channel at the outflow boundary condition and pressure is kept fixed over that face. The initial velocity is given by

$$\mathbf{U}(0,x,y,z)=\begin{pmatrix}4y(1-y)\\0\\0\end{pmatrix}+C_{\text{noise}}\begin{pmatrix}-4\pi\sin(4\pi y)\\-3\pi\sin(3\pi z)\\3\pi\cos(3\pi x)\end{pmatrix} \tag{28}$$

Without the presence of any noise in the initial condition ($C_{\text{noise}}=0.0$),

$$\mathbf{U}(t,x,y,z)=\begin{pmatrix}4y(1-y)\\0\\0\end{pmatrix} \tag{29}$$

$$P(t,x,y,z)=-8\nu(x-10)+P_0 \tag{30}$$

is a solution of the Navier–Stokes equations (4–6). The total kinetic energy of the flow inside the channel (steady condition) is estimated to be 2.666 by integrating the velocity distribution given by Eq. (29) over the entire nondimensionalized domain.

The nondimensional molecular viscosity is assumed to be $\upsilon=10^{-5}$, and the Reynolds number of the flow is based on the average inflow velocity and the height of the channel L:

$$Re=\frac{\bar{U}L}{\upsilon}=\frac{2}{3}10^5\approx 66,667 \tag{31}$$

In this simulation, the Mach number is set to the value of 0.01 to keep the flow regime close to incompressible. The total kinetic energy of the computational domain is computed by

$$E(t)=\sum_{n=1}^{N}\left(\left(\sum_{i=1}^{3}\frac{u_i^2(n)}{2}\right)\times\text{vol}(C_n)\right) \tag{32}$$

where N is defined as the total number of nodes inside the domain, and $\text{vol}(C_n)$ is the volume of cell C_n, which belongs to node n.

In the channel flow simulation, γ is assumed to be chosen within a range with fixed limits for each simulation. The limits of that range fall within [0, 1]. This makes it possible to adjust the average effect of upwinding in every test case. To test the stability of the self-adaptive scheme, the permitted intensity of the local wiggles (θ) is set to zero, intended to completely damp the local wiggles. Considering that the grid resolution is very low and θ has been set to zero, we expect a laminar solution despite the fact that the Reynolds number is relatively high.

Different computations, as summarized in Table 1, are performed to evaluate the stability of the scheme against strong fluctuations that might be present in every typical LES.

When full upwinding (case 1) is considered, the total kinetic energy of the system is somewhat lower than the expected value of 2.666. Recall that the flow is not resolved well enough by the mesh, and Eq. (32) is therefore not a good approximation for the integration operation used to calculate the estimated total kinetic energy. In cases 2, 3, and 4, the lower limit of the upwinding parameter γ is decreased (Table 1), and it reduces the average effects of upwinding. By decreasing γ, the flux calculation scheme becomes more central, which makes the simulation more unstable, and therefore the wiggles gradually start to appear inside the domain. The self-adaptive scheme tries to locally adjust γ to damp those wiggles, and as a result, the simulation still remains stable. However, a gradual increase in the total kinetic energy is observed, as illustrated in Fig. 5. In case 4, the effects of those random wiggles appear even further and the total kinetic energy is showing chaotic fluctuations. That is an indication of a fairly unstable flow regime present inside the channel, even though the total kinetic energy has still remained bounded. In case 2, the total kinetic energy becomes very close to 2.666; therefore, for the next part of this test, the lower limit of the upwinding term is kept equal to 0.43. In Fig. 6, the effect of initial noise is investigated using cases 2, 5, and 6. As shown in the graph, the self-adaptive upwinding method is showing a very good stability characteristic, despite the fact that the value of 0.1 for the noise coefficient is 10 times higher than the value used in [17].

B. Decaying Isotropic Turbulence

The simplest kind of turbulence is isotropic; therefore, isotropic turbulence forms a natural starting point for the study and simulation of turbulence. This flow has been considered in many earlier and recent investigations [18–23]. The experiment regarding the decay of isotropic turbulence by Comte-Bellot and Corrsin (CBC) [24] is used to validate our simulation. In the experiment, turbulence was generated using a biplane square-rod grid with mesh size $M=$ 5.08 cm, which was placed inside a flow with the uniform velocity of $U_0=10$ m/s. The Reynolds number based on the grid spacing is $Re_M=U_0M/\nu=34,000$. The measurements were performed downstream of the grid at three consecutive stations ($U_0t_{\text{CBC}}/M=$ 42, 98, and 171). The dimensional time in the experiment (t_{CBC}) is defined as

$$t_{\text{CBC}}=\int_0^x\frac{\mathrm{d}x}{U(x)} \tag{33}$$

where x is the downstream distance from the grid and $U(x)$ is the mean velocity. Because the same flow passes through all the stations, we can use the measured data to verify the validity of the numerical results at three different computational times. The simulation is carried out inside a box with a size larger than the integral length scale

Table 1 Explanation of different cases for channel flow simulation

Case no.	θ	Upwinding parameters Upper value	 Lower value	C_{noise}	C_S	$E(t)$ $t=0$	 $t=10$
1	0.0	1.0	1.0	0.0	0.0	2.6617	2.3296
2	0.0	1.0	0.43	0.0	0.0	2.6617	2.6508
3	0.0	1.0	0.1	0.0	0.0	2.6617	2.9446
4	0.0	1.0	0.0	0.0	0.0	2.6617	3.0023
5	0.0	1.0	0.43	0.01	0.0	2.73813	2.6510
6	0.0	1.0	0.43	0.1	0.0	10.2229	2.6738

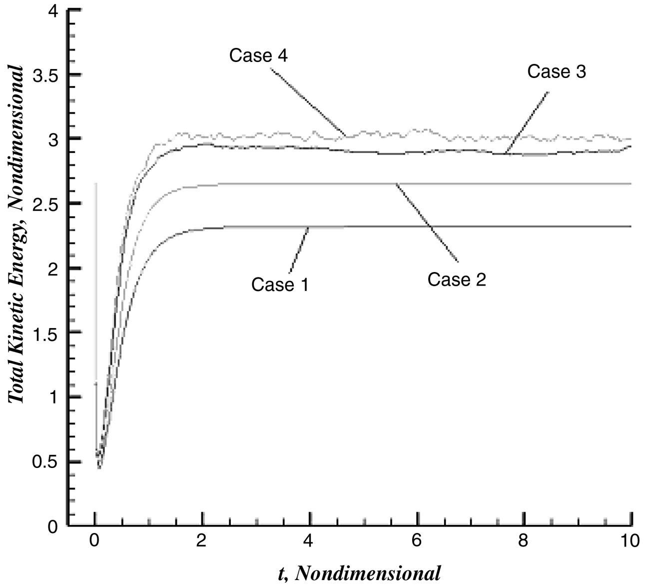

Fig. 5 Channel flow simulation (cases 1, 2, 3, 4).

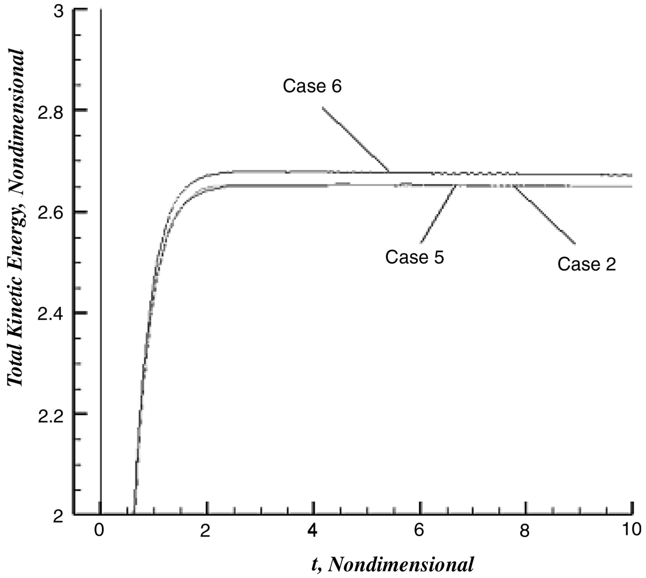

Fig. 6 Channel flow simulation (cases 2, 5, 6).

and much smaller than the wind tunnel's cross section. This model uses 32,768 nodes and 17,8746 tetrahedrons. Each edge of the box is divided by 32 nodes into segments of equal size and then all elements are distributed uniformly inside the domain. A periodic boundary condition is imposed on all sides of the box.

In [24], a one-dimensional energy spectrum E_{11} at $U_0 t_{\mathrm{CBC}}/M = 42$ is reported, which can be approximated by a logarithmic polynomial as [18,25]

$$\log_e E_{11}(k) = A_0 + A_1 \log_e k + A_2 (\log_e k)^2 + A_3 (\log_e k)^3 + A_4 (\log_e k)^4 \tag{34}$$

Table 2 Coefficients of the energy spectrum at $U_0 t_{\mathrm{CBC}}/M = 42$

Coefficient	Value
A_0	4.7935398
A_1	−1.3284141
A_2	−0.2146974
A_3	−0.0314604
A_4	−0.0169870

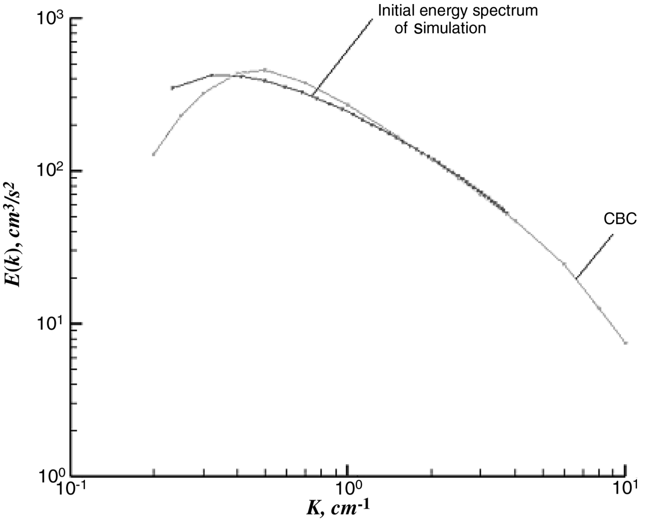

Fig. 7 Energy spectrums at $U_0 t_{\mathrm{CBC}}/M = 42$.

In the isotropic turbulence, the energy spectrum $E(k)$ can be obtained from $E_{11}(k)$ by

$$E(k) = \frac{1}{2} k^3 \frac{\partial}{\partial k}\left(\frac{1}{k}\frac{\partial E_{11}}{\partial k}\right) \tag{35}$$

This yields

$$E(k) = E_{11}\left\{\frac{1}{2}\left[A_1 + 2A_2 \log_e k + 3A_3 (\log_e k)^2 + 4A_4 (\log_e k)^3\right]^2 + A_2 - A_1 + (3A_3 - 2A_2)\log_e k + (6A_4 - 3A_3)(\log_e k)^2 - 4A_4 (\log_e k)^3\right\} \tag{36}$$

for which the coefficients are reported in Table 2.

The initial velocity field for the simulation is created by superimposing the Fourier modes that prescribe the energy spectrum given in Eq. (36) but have random phases (Fig. 7). The method has been described in [18,25]. The initial pressure distribution is obtained from the incompressible Poisson equation using the initial velocity field. A slight difference is present between $E(k)$ reported by CBC data [24] and the applied initialization for $E(k)$, as shown in Fig. 7. Note that during the CBC experiment, one-dimensional energy spectrums $E_{11}(k)$ were measured at three different locations, and then the affiliated energy spectrums $E(k)$ were calculated using graphical differentiation of faired curves. It seems that using polynomial curve fitting, which is implemented here, is more accurate than the CBC method. That is, however, the case only for $U_0 t_{\mathrm{CBC}}/M = 42$. Our attempts to use the polynomial procedure to extract $E(k)$ from $E_{11}(k)$ for $U_0 t_{\mathrm{CBC}}/M = 98$ and $U_0 t_{\mathrm{CBC}}/M = 171$ did not achieve any better result in comparison with CBC. Therefore, we decided to initialize the simulation using Eq. (36), whereas for comparing the energy spectrum of different simulations at $U_0 t_{\mathrm{CBC}}/M = 98$ and $U_0 t_{\mathrm{CBC}}/M = 171$ with the experiment, the curves provided by CBC are used.

As mentioned earlier, the decaying turbulence is simulated by considering the fluid to be inside a cube. Each side of this cube has the length of L_C, which is assumed to be equal to 43.787 cm. This length represents the zero intercept of $E(k)$ in Eq. (36).

The length scale $L_\infty = 6.96889$ cm and $U_\infty = 3420$ cm/s are chosen for nondimensionalization of the governing equations (4–6); therefore, the dimensionless length of the cube's edges becomes equal to 2π [18]. $E(k)$ and k have been nondimensionalized by $U_\infty^2 L_\infty$ and L_∞^{-1}, respectively. The dimensionless time of the simulation (t) is related to t_{CBC} by

$$t = \left(\frac{U_0 t_{\mathrm{CBC}}}{M} - 42\right)\frac{M}{U_0}\frac{U_\infty}{L_\infty} \tag{37}$$

Table 3 Parameters used in different test cases for decaying turbulence simulation

Case no.	Upwinding parameters Upper value	 Lower value	θ	C_S
1	1.0	1.0	——	0.01
2	1.0	0.0	0.0	0.01
3	1.0	0.0	−0.00001	0.01
4	1.0	0.0	−0.0001	0.01
5	1.0	0.0	−0.0001	0.1
6	1.0	0.0	−0.0001	1.0

and thus

$$t = 2.493\left(\frac{U_0 t_{\mathrm{CBC}}}{M} - 42\right) \tag{38}$$

The flow in the experiment is essentially incompressible. The turbulence Mach number M_t of the initialization is equal to $0.98959541 \times 10^{-3}$, where

$$M_t = \sqrt{\overline{u_i u_i}}/a_\infty \tag{39}$$

and $a_\infty = 3420\ \mathrm{cm/s}$.

In earlier works, spectral methods have been mainly used for LES of decaying turbulence [19,21,22,25,26]. The numerical dissipation was relatively negligible, and the SGS model has therefore been the main factor to determine the overall dissipation of the simulation. Other numerical methods, however, are not usually as accurate as spectral methods, and it is therefore not possible to use the overall judgment to estimate the relative importance of the numerical dissipation. There have been cases reported in the literature in which the numerical dissipation of the method was found to be fairly significant.

For example, in [27], compressible isotropic turbulence at zero molecular viscosity using a wide set of schemes, including a total-variation-diminishing MUSCL scheme (third order) was studied. They concluded that the numerical dissipation affected the entire spectrum and MUSCL was found to be too dissipative at 64^3. Another example would be [8], in which the numerical method was based on a finite volume discretization using the MUSCL solver. A self-adaptive method was implemented to decrease the over-dissipative nature of the MUSCL method and it gave acceptable results for 32^3. It was reported that the original scheme was overdissipative, and for a 32^3 grid, the numerical dissipation was dominant over the subgrid-scale dissipation.

Considering the given discussion, one of the main concerns in this work is to study the effects of numerical dissipation of the Roe-MUSCL scheme and to introduce a method (self-adaptive upwinding) to control its undesirable influence. To study the effects of the self-adaptive upwinding, test cases described in Table 3 are considered. Case 1 shows the set of conditions representing full upwinding. The numerical dissipation is found to be very high (Fig. 8), and it is therefore necessary to significantly decrease the upwinding effect.

In cases 2, 3, and 4, the effect of self-adaptive upwinding is demonstrated. In case 2, the self-adaptive upwinding flag is activated, and the $E(t)$ graph is therefore significantly closer to CBC data points (Fig. 8). In this case, θ is set to 0.0, which means that the self-adaptive scheme tries to dissipate the wiggles in low length scales (Fig. 9). Of course, in principle, this somehow contradicts the idea of LES, in which energy stored at higher modes is expected to play a role in the simulation. Therefore, in the next test cases, θ is decreased, with the hope that it will improve the energy distribution in the highest modes. In case 3, θ is decreased to −0.00001, and total kinetic energy therefore becomes a very good match for the experimental data. Results of case 4, however, show that the $E(t)$ graph can even elevate further upward by decreasing the θ further. In this case, the slope of the energy spectrum is a better match for the CBC data, even though the total kinetic energy is clearly higher than the experimental predictions.

As shown in Figs. 9 and 10, the energy is cascaded from lower modes toward higher modes. The energy spectrum is showing a dissipative nature at higher modes, whereas it is not dissipative enough in relatively low modes, and an undesired overshoot is present. By decreasing θ, not only is the energy in the higher modes increases, but some energy in the lower modes is also accumulated; therefore, it is difficult to achieve a complete match between numerical and experimental data, as shown in the case of spectral methods.

In cases 4, 5, and 6, the effect of explicit SGS is studied (Figs. 11–13). By increasing the Smagorinsky constant, the energy in the domain is more dissipated, and that results in different levels of $E(t)$, as shown in Fig. 11. We conclude that the self-adaptive upwinding scheme has significantly improved the results, as explained previously. It was also found that the overall dissipative nature of simulation is affected by both the SGS model and the numerical method.

C. Flow Separation Detection over NACA0025

In this section, we want to investigate the performance of the self-adaptive scheme for the simulation of flow separation over an airfoil, which is a more challenging problem. The experimental data of

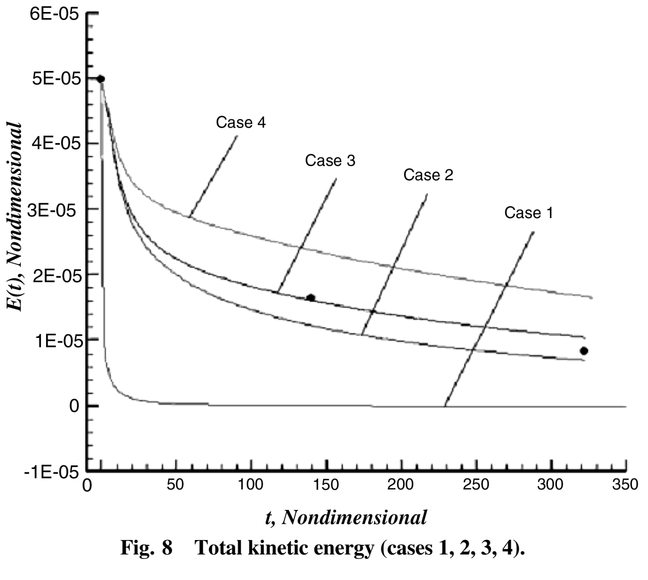

Fig. 8 Total kinetic energy (cases 1, 2, 3, 4).

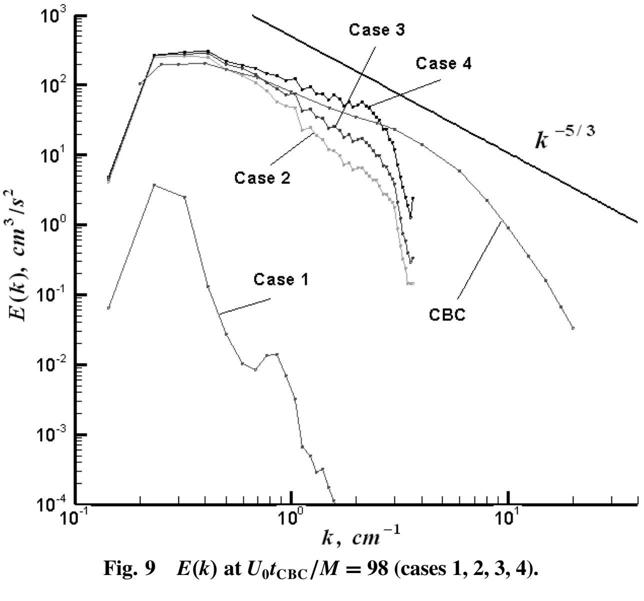

Fig. 9 $E(k)$ at $U_0 t_{\mathrm{CBC}}/M = 98$ (cases 1, 2, 3, 4).

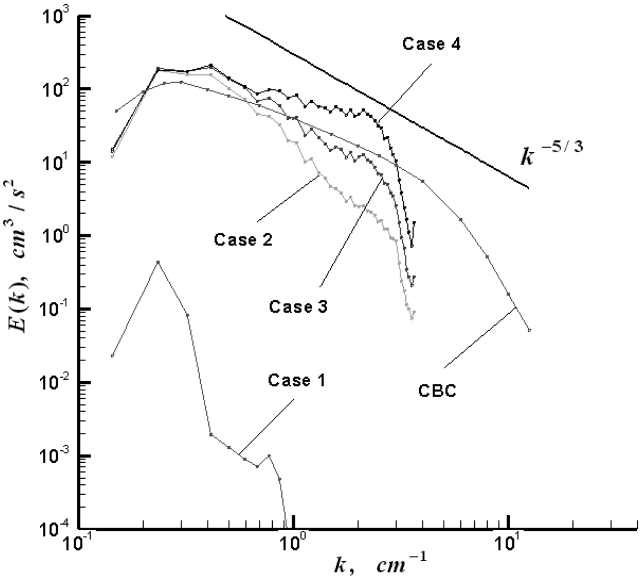

Fig. 10 $E(k)$ at $U_0 t_{\mathrm{CBC}}/M = 171$ (cases 1, 2, 3, 4).

Yarusevych [28] are used to validate the simulation of the flow around a NACA0025 profile. Yarusevych investigated the separation phenomenon on the upper surface of the NACA0025 airfoil at a Reynolds number equal to 100,000. The experiment was conducted in a low-turbulence recirculating wind tunnel at the University of Toronto. The wind tunnel has a 5-m-long octagonal test section with a span of 0.91 m and a height of 1.215 m. The airfoil is mounted horizontally inside the wind tunnel, 0.4 m downstream of the contraction section. The airfoil's surface is equipped with 65 pressure taps to measure the pressure distribution along the upper and lower surfaces in the midspan. Further details about the experiment can be found in [28,29].

In our simulation, the objective is to verify the ability of the proposed scheme to predict the location of the separation point and to capture the recirculation zone. The simulation is carried out in a flow with the chord Reynolds number (Re_C) of 100,000 and at angles of attack equal to 0 and 5 deg. The chord length is considered to be 0.3 m, as in the experiment. The span length is chosen to be one chord, to avoid the wall's effects at midspan, although it is 0.15 × chord in the experiment. The computational domain has 0.5 × chord upstream of the leading edge and one chord downstream of the trailing edge. The height of the test section is 4 × chord, equal to the height of the wind tunnel.

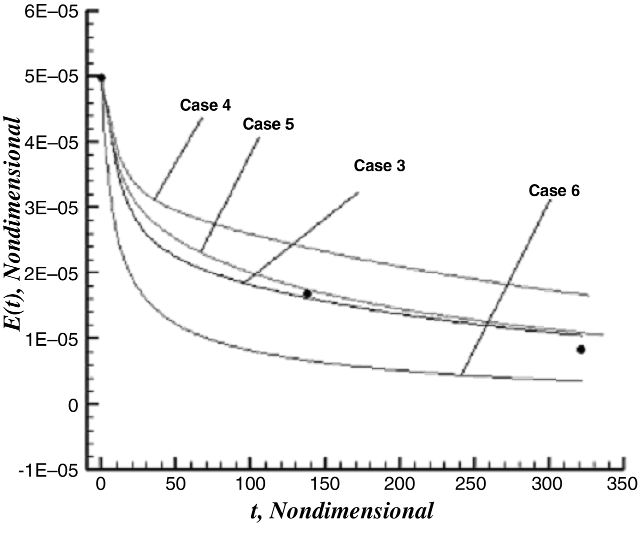

Fig. 11 Total kinetic energy (cases 3, 4, 5, 6).

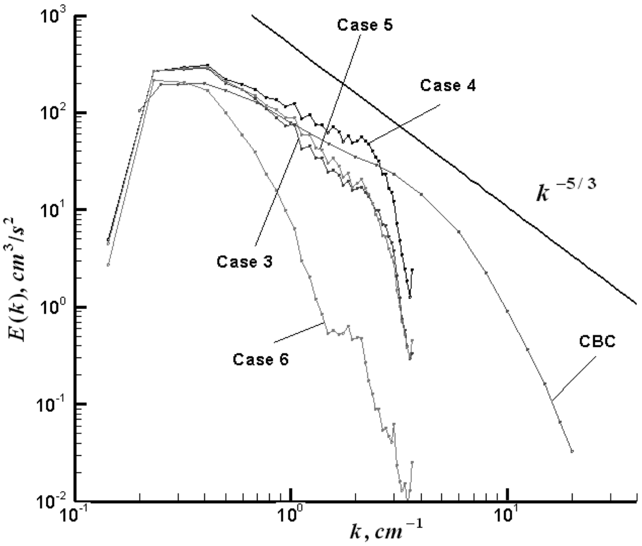

Fig. 12 $E(k)$ at $U_0 t_{\mathrm{CBC}}/M = 98$ (cases 3, 4, 5, 6).

To accurately capture the separation phenomenon over the upper surface of the wing, a very fine boundary-layer mesh has been generated. It is compromised of 50 layers of structured mesh with the ratio of 1.05, which smoothly mixes with the grids outside of the boundary layer. Mesh resolution for LES in the regions near the solid walls is usually assumed to be on the order of unity in the normal direction ($\Delta y^+ \approx 1$), to accurately resolve the velocity gradients [30]. In this simulation, two models with different mesh resolutions are generated. The model with the finer mesh has the resolution of $\Delta y^+ \approx 1$ and $\Delta x^+ = \Delta z^+ \approx 20$ (streamwise and spanwise spacing) at the boundary-layer regions, whereas the coarser mesh has the minimum grid size of $\Delta y^+ \approx 10$. As will be shown later, the coarse mesh does not capture the separation phenomenon at all. The largest edges inside both grids have a length equal to

$$\Delta x^+ = \Delta y^+ = \Delta z^+ \approx 100$$

in the far-field regions. This helps to have the required resolution near the solid walls. The fine mesh is composed of about 3 million nodes and 9.5 million elements and is decomposed into 64 subdomains to be run in parallel.

As for the boundary conditions, the velocities and density are imposed at the inflow plane. There are four variables that are assigned according to far-field properties, and one comes from

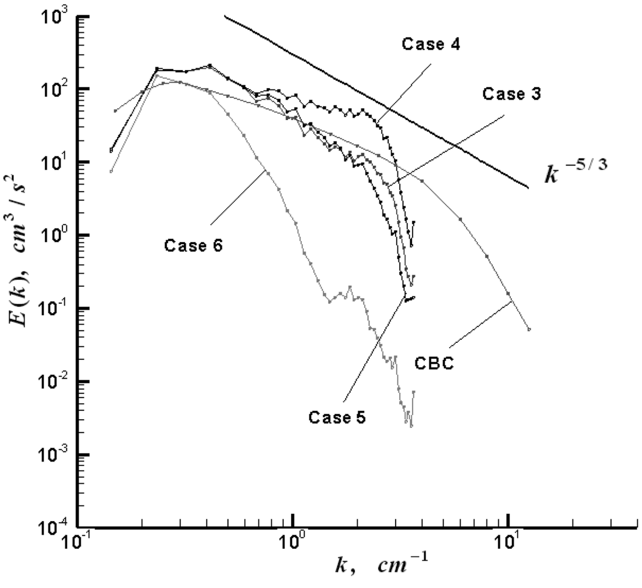

Fig. 13 $E(k)$ at $U_0 t_{\mathrm{CBC}}/M = 171$ (cases 3, 4, 5, 6).

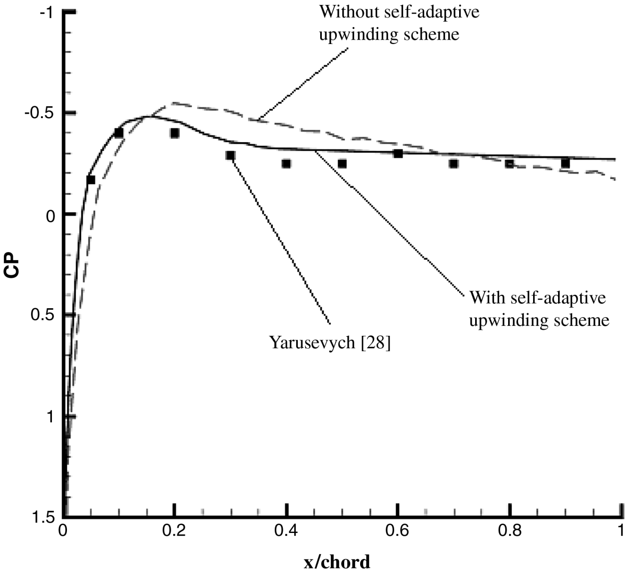

Fig. 14 Pressure coefficient over the upper surface ($\alpha = 5\,\mathrm{deg}$, fine mesh).

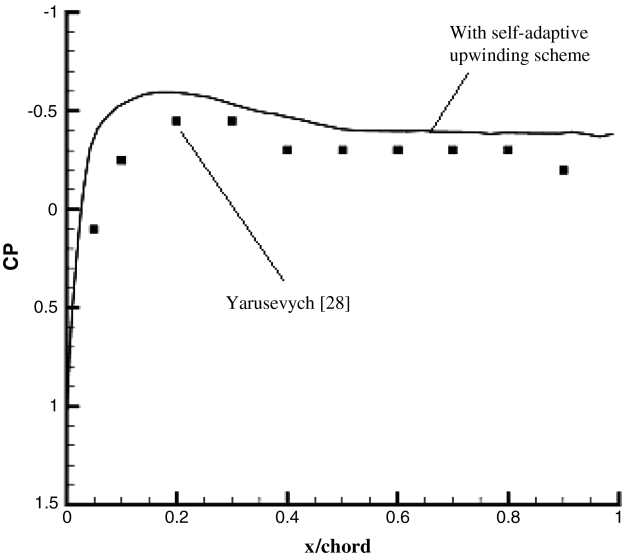

Fig. 16 Pressure coefficient over upper and lower surfaces ($\alpha = 0\,\mathrm{deg}$, fine mesh).

the numerical solution at the inlet. At the outflow plane, static pressure is fixed; therefore, one variable is set according to the physical domain and the remaining four variables are calculated from the numerical solution. For this simulation, the streamwise velocity distribution is set to $u = U_\infty \cos\alpha$, and the velocity distribution in the two spanwise directions is set to $v = 0$ and $w = U_\infty \sin\alpha$, respectively. The freestream velocity is shown by U_∞, and α represents the angle of attack. On the solid walls (airfoil surface and channel walls), a zero-velocity condition is applied in all directions to the surface. In addition, to avoid the influence of heat transfer through the walls, the adiabatic boundary condition is applied to the solid walls.

In the simulation, the time step is controlled by the CFL number, which linearly increases from 1 to 5; therefore, the maximum CFL is limited to 5 and the maximum time step is set to be $\Delta t = 0.0001$ s. The simulation continues running until the flow becomes statistically steady. The best way to make sure that the flow is fully developed and steady is to examine the time history of the residuals and the forces on the airfoil. Afterward, the sampling data statistics are extracted. The simulation is continued for a period of time and the quantities are averaged. This period is much longer than the period of flow oscillations.

According to the results, when the angle of attack is equal to 5 deg and the self-adaptive upwinding method is not active (full upwinding), separation is not captured and all the streamlines in the flowfield follow the airfoil's surface. When the self-adaptive upwinding is activated, the flow separation occurs on the upper surface of the airfoil and the recirculation zone is generated; however, it fails to reattach. As shown, the flow separates on the upper surface of the airfoil and fails to reattach. The separation point is the specific location over the wing at which the boundary layer tends to separate from the solid body as a result of the local adverse pressure gradient.

In Fig. 14, the pressure coefficient C_P is plotted against the distance from the leading edge of the airfoil at Reynolds number of 100,000 and $\alpha = 5\,\mathrm{deg}$. As shown, the original scheme (with full upwinding) is not able to capture the separation, and the flow remains attached to the wing. The self-adaptive upwinding method shows its positive influence by decreasing the numerical dissipation and allowing the separation to take place.

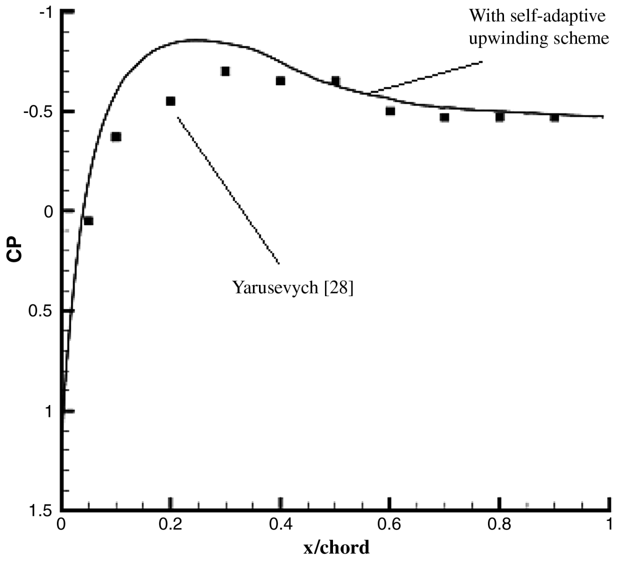

Fig. 15 Pressure coefficient over the lower surface ($\alpha = 5\,\mathrm{deg}$, fine mesh).

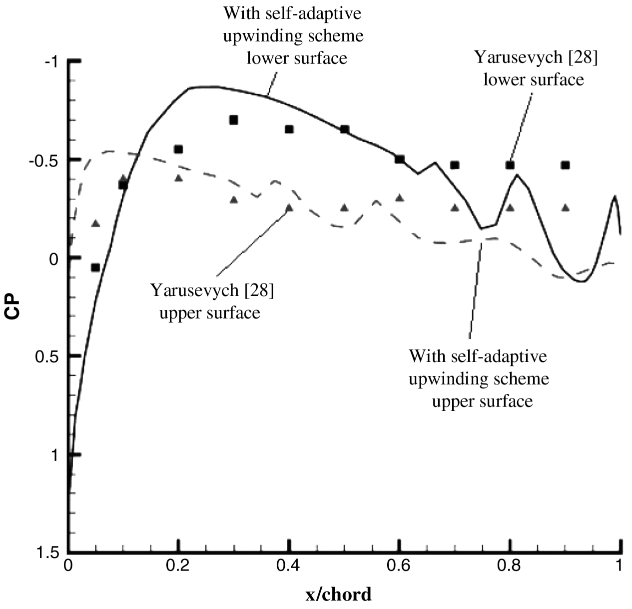

Fig. 17 Pressure coefficient over the upper and lower surfaces ($\alpha = 5\,\mathrm{deg}$, coarse mesh).

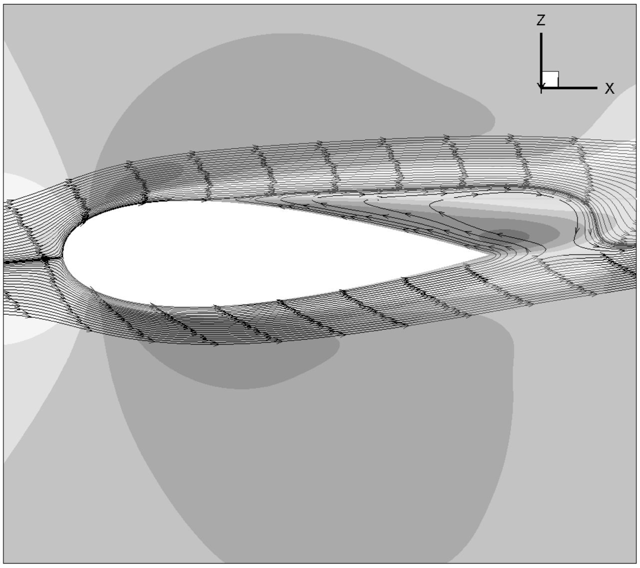

Fig. 18 Streamlines and velocity contours at time = 1.0 s.

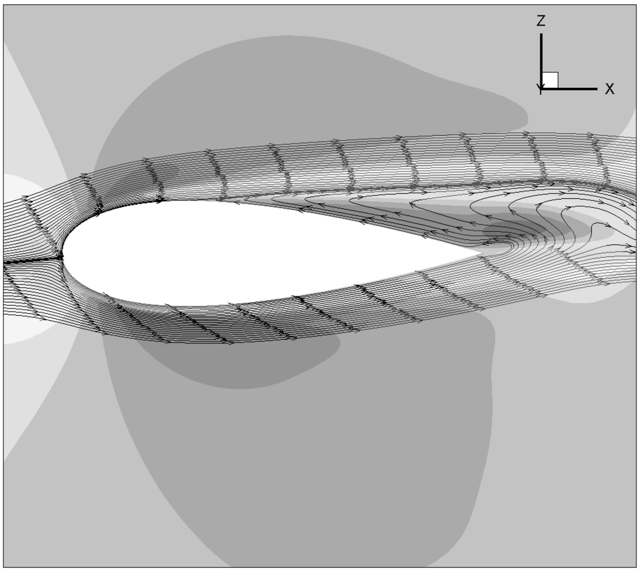

Fig. 19 Streamlines and velocity contours at time = 1.015 s.

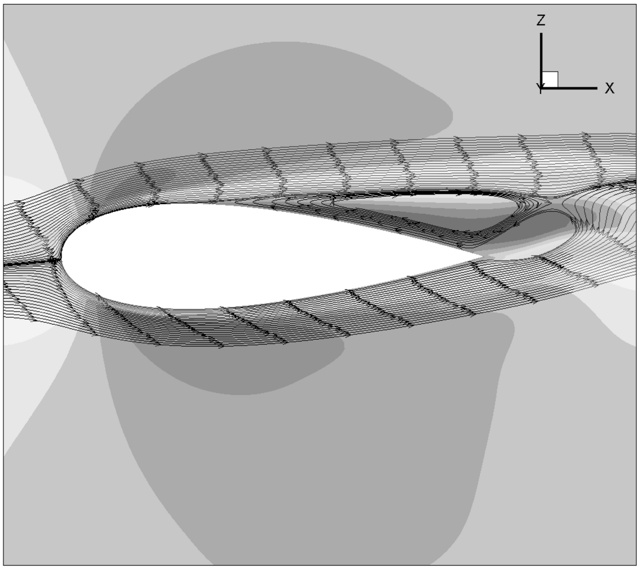

Fig. 20 Streamlines and velocity contours at time = 1.033 s.

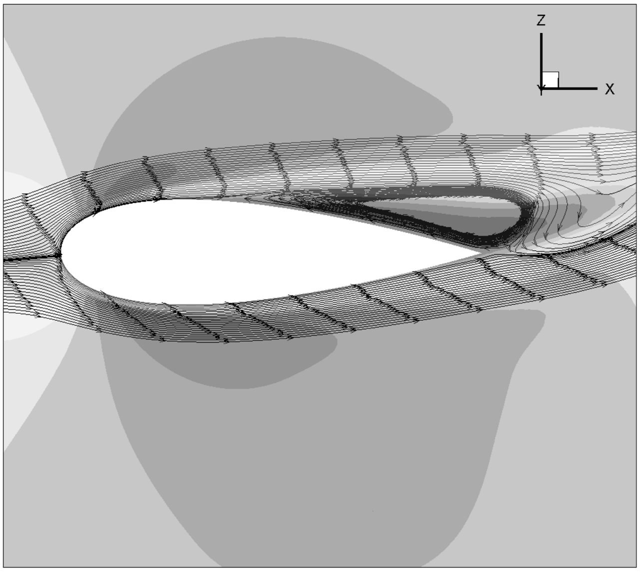

Fig. 21 Streamlines and velocity contours at time = 1.049 s.

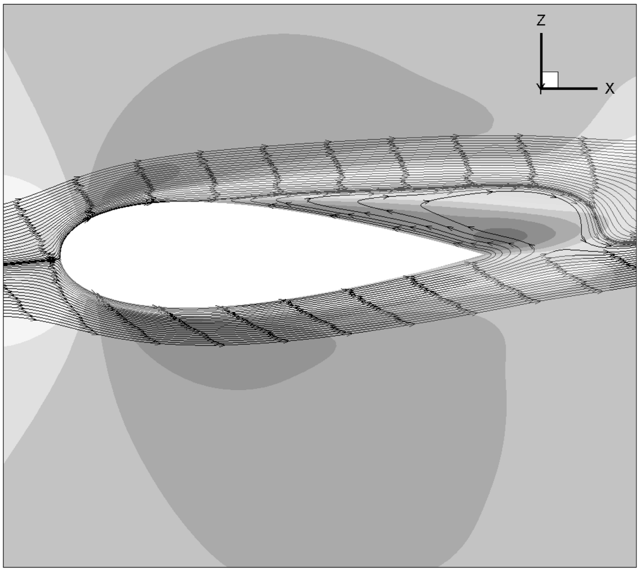

Fig. 22 Streamlines and velocity contours at time = 1.067 s.

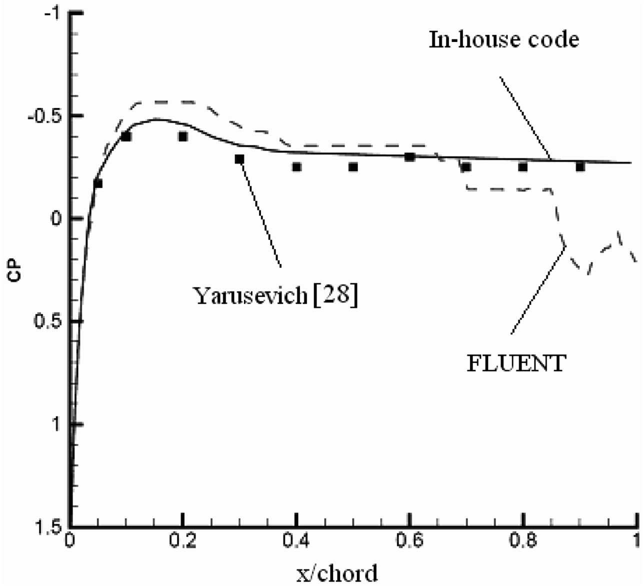

Fig. 23 Upper surface pressure distribution at $\alpha = 5\,\mathrm{deg}$.

The location of separation for the angle of attack equal to 5 deg is estimated to be around $x/\text{chord} = 0.31$, whereas the experimental data reports $x/\text{chord} = 0.30$ for the separation location at the same angle of attack. As shown in this graph, the region downstream of the separation point has almost constant pressure. Because the boundary layer does not reattach to the airfoil's surface downstream of the separation point, constant pressure region extends up to the trailing edge. However, the separation point moves toward the trailing edge as the angle of attack is decreased. The pressure coefficient over the lower surface of the wing is shown in Fig. 15.

In Fig. 16, the pressure coefficient is plotted for $\alpha = 0$ deg. As expected, due to the symmetrical profile of the airfoil and zero incidence angle of attack, the upper and lower pressure distributions overlap. The boundary layer separates at approximately $x/\text{chord}=$ 0.48, whereas the experiment reported it to happen at $x/\text{chord}=$ 0.37.

The ability to capture the separation phenomenon seems to have a direct relation to the mesh resolution as well. In Fig. 17, the pressure coefficient for the coarse mesh over the upper and lower surfaces using self-adaptive upwinding scheme is reported. As shown, the simulation on the course mesh is not able to capture the separation.

One of the features of LES in respect to RANS is its capability to capture unsteady motions. The unsteady development of the separated shear layer and the periodic vortex shedding are considered to be among the important features of this simulation [31]. Therefore, for better understanding of the unsteady flow in the separated region, instantaneous streamlines and velocity contours for different simulation times are shown for one shedding cycle in Figs. 18–22. The time step is fixed at 0.0001 s. Because the flow is unsteady, the streamlines are changing with time, and the vortex shedding can be observed at the trailing-edge region. As shown in these figures, the cycle starts in Fig. 18 at 1.0 s and terminates in Fig. 22 at 1.067 s. This shows that a complete vortex-shedding period takes almost 0.067 s, based on our simulation.

To highlight the enhanced capabilities of the code presented here, the same flow conditions are simulated using a standard computational fluid dynamics (CFD) commercial code. FLUENT is chosen as the CFD tool because its LES capability has been upgraded in version 6.2 with several enhancements in SGS modeling and also in its numerics, such as bounded central differencing and noniterative time advancement.

As for the boundary conditions, outflow boundary condition is used because the details of the flow velocity and pressure are not known before the solution of the flow problem. A velocity inlet boundary condition is applied to define the flow velocity, along with all relevant scalar properties of the flow, at the inlet.

Table 4 Comparison of used parameters in different numerical simulations

Numerical tool	Compressible code	FLUENT
Number of nodes	3,000,000	5,800,000
Number of elements	9,500,000	18,000,000
Degrees of freedom	5 × 3 million	5 × 18 million
Δy^+	≈ 1	≈ 0.2
No. of CPUs	64	16
C_S	0.00014	0.00014
Upwinding parameters		
Upper value	1.0	——
Lower value	0.0	——
θ	−0.0001	——

As FLUENT's user guide recommends, simulation is started by running a steady-state flow simulation using a RANS turbulence model (standard k-ε model) with a small CFL number. Simulation is continued until the flowfield is reasonably converged. In the next step, an appropriate time-step size and the other required solution parameters are set and the LES option is enabled. The simulation is continued until the flow becomes statistically steady. In this stage, the initial statistics are zeroed out and data sampling is enabled to get statistically stable data. The same mesh that was previously used for the compressible in-house code was chosen at first for the simulation with FLUENT; however, it could not capture the separation at $\alpha = 5$ deg. Therefore, another mesh with finer resolution inside the boundary layer was generated ($\Delta y^+ \approx 0.2$). For this mesh, the first separation bubbles were detected at $x/\text{chord} = 0.42$ for $\alpha = 5$ deg, as shown in Fig. 23. The surface pressure distributions are acceptable around the leading edge; but for x/chord larger than 0.6, even though we expect a constant static pressure as was predicted by the in-house code and also by the experiment, the pressure decreases on both the upper and the lower surfaces. This behavior is the result of reattachment of the flow to the surface of the wing that is not physical and therefore introduces a significant error. The difference between experimental data and the FLUENT simulation is even more significant in Fig. 24, in which the pressure distribution on the lower surface of the wing is shown.

In conclusion, we can say that the results of the proposed scheme have been more accurate and reliable than the results of the simulation by FLUENT, despite the fact that the grid used in the later simulation was much finer than that used for the simulation with the in-house code. As shown in Table 4, FLUENT's mesh is almost 2 times more refined in terms of the number of nodes in comparison with the mesh used by the in-house code. The surface pressure for $\alpha = 0$ deg is also shown in Fig. 25. Note that in FLUENT, control volumes are the same as grid elements, whereas the in-house code uses node-centered control volumes for the calculations, and

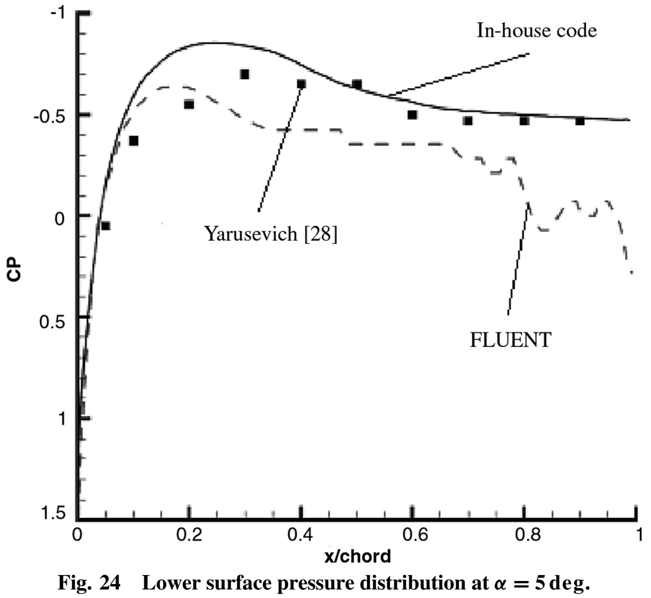

Fig. 24 Lower surface pressure distribution at $\alpha = 5$ deg.

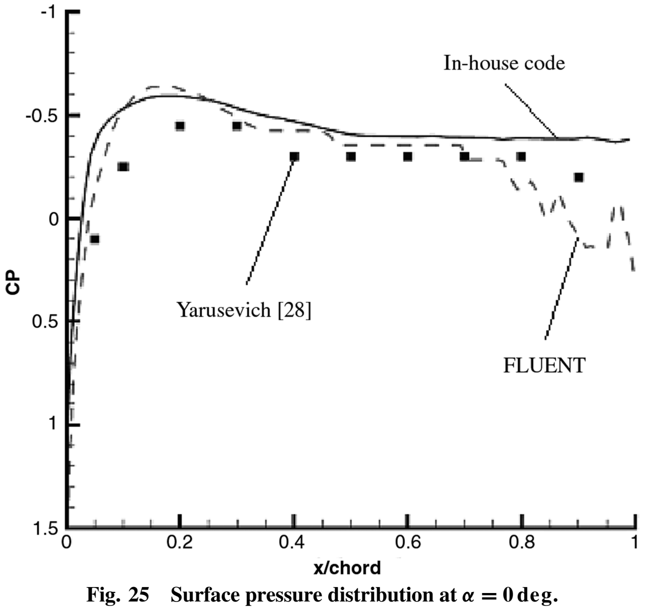

Fig. 25 Surface pressure distribution at $\alpha = 0$ deg.

therefore the required degrees of freedom are 6 times more for FLUENT in comparison with the in-house code.

V. Conclusions

A self-adaptive upwinding method for an unstructured finite volume flow solver has been presented. The scheme tries to regulate the numerical dissipation, relying on adjustment of the upwinding term and a sensor that detects the intensity of wiggles in the flow variables. It was firstly used in a channel flow simulation to test its stability. It showed very good stability characteristic, even when the noise coefficient was very high. Second, isotropic turbulence was considered. The original scheme appeared to be overdissipative, preventing SGS model from producing a proper LES solution. The self-adaptive upwinding method, however, improved the decaying behavior of total kinetic energy in time and also improved the slope of the energy spectrum. The wiggle detector made it possible to adjust the amount of energy in the highest modes and therefore improved the results. That adjustment, however, influenced the energy distribution on the entire spectrum and showed some undesirable effects in the lower modes. Finally, the flow separation phenomenon over a NACA0025 profile at angles of attack equal to 0 and 5 deg has been investigated. The original flux calculation scheme appeared to be overdissipative, preventing the flow from separating over the airfoil. The self-adaptive upwinding method reduced the artificial diffusion to the level of flow instability and made it possible for the separation to occur. The proposed scheme produced results that are comparable with experimental data and also more accurate and reliable than results obtained by FLUENT, despite the fact that the grid used in the later simulation was much finer than that used for the simulation with the in-house code.

References

[1] Spyropoulos, E. T., and Blaisdell, G. A., "Large-Eddy Simulation of a Spatially Evolving Supersonic Turbulent Boundary Layer Flow," *AIAA Journal*, Vol. 36, No. 11, 1998, pp. 1983–1990. doi:10.2514/2.325

[2] Mary, I., and Sagaut, P., "Large Eddy Simulation of Flow Around an Airfoil Near Stall," *AIAA Journal*, Vol. 40, No. 6, 2002, pp. 1139–1145. doi:10.2514/2.1763

[3] Andersson, N., Eriksson, L. E., and Davidson, L., "Large-Eddy Simulation of a Subsonic Turbulent Jets and Their Radiated Sound," *AIAA Journal*, Vol. 43, No. 9, 2005, pp. 1899–1912. doi:10.2514/1.13278

[4] Hahn, M., and Drikakis, D., "Large Eddy Simulation of Compressible Turbulence Using High-Resolution Methods," *International Journal for Numerical Methods in Fluids*, Vol. 47, Nos. 8–9, 2005, pp. 971–977. doi:10.1002/fld.882

[5] Carpentier, R., "Comparaison Entre des Schémas 2D de Type Roe Sur Maillages Régulier Triangle ou Quadrangle, 2: Calcul au Sommet-le bg Schéma," *Rapports de Recherche*, Inst. National de Recherche en Informatique et en Automatique, Rept. 3360, Valbonne, France, 1998.

[6] Bui, T. T., "A Parallel, Finite-Volume Algorithm for Large Eddy Simulation of Turbulent Flows," NASA Dryden Flight Research Center, TM-206570, Edwards AFB, CA, Jan. 1999.

[7] Camarri, S., and Salvetti, M. V., "Large-Eddy Simulation of a Bluff-Body Flow on Unstructured Grids," *International Journal for Numerical Methods in Fluids*, Vol. 40, No. 11, 2002, pp. 1431–1460. doi:10.1002/fld.425

[8] Ciardi, M., Saugaut, P., Klein, M., and Dawes, W. N., "A Dynamic Finite Volume Scheme for Large-Eddy Simulation on Unstructured Grids," *Journal of Computational Physics*, Vol. 210, No. 2, 2005, pp. 632–655. doi:10.1016/j.jcp.2005.04.025

[9] Ferziger, J. H., "Direct and Large Eddy Simulation of Turbulence," *Numerical Methods in Fluid Mechanics*, CRM Proceedings and Lecture Notes, Vol. 16, Centre de Recherches Mathématiques, Montréal, and American Mathematical Society, Providence, RI, 1998, pp. 53–77.

[10] Camarri, S., Salvetti, M. V., and Koobus, B., "A Low-Diffusion MUSCL Scheme for LES on Unstructured Grids," *Computers and Fluids*, Vol. 33, No. 9, 2004, pp. 1101–1129. doi:10.1016/j.compfluid.2003.10.002

[11] Dahlström, S., and Davidson, L., "Large Eddy Simulation Applied to a High Reynolds Flow Around an Airfoil Close to Stall," 41st AIAA Aerospace Sciences Meeting and Exhibit, AIAA Paper 2003-776, 2003.

[12] Hirsch, C., *Numerical Computation on Internal and External Flows*, Vol. 1, Wiley, Hoboken, NJ, 1988.

[13] Cadiou, A., "NadiaLES: Theoretical Manual," Centre National De La Recherche Scientifique, Rept. LMFA-UMR CNRS 5509, Ecully Cedex, France, 2003.

[14] Larcheveque, L., Sagaut, P., Mary, I., and Labbé, O., "Large-Eddy Simulation of a Compressible Flow Past a Deep Cavity," *Physics of Fluids*, Vol. 15, No. 1, 2003, pp. 193–210. doi:10.1063/1.1522379

[15] Quéméré, P., and Sagaut, P., "Zonal Multi-Domain RANS/LES Simulations of Turbulent Flows," *International Journal for Numerical Methods in Fluids*, Vol. 40, No. 7, 2002, pp. 903–925. doi:10.1002/fld.381

[16] Hallo, L., LeRibault, C., and Buffat, M., "An Implicit Mixed Finite-Element-Finite-Volume Method for Solving 3-D Turbulent Compressible Flows," *International Journal for Numerical Methods in Fluids*, Vol. 25, No. 11, 1997, pp. 1241–1261. doi:10.1002/(SICI)1097-0363(19971215)25:11<1241::AID-FLD595>3.0.CO;2-1

[17] John, V., *Large Eddy Simulation of Turbulent Incompressible Flows*, Springer–Verlag, Berlin, 2004.

[18] Knight, D., Zhou, G., Okong'o, N., and Shukla, V., "Compressible Large Eddy Simulation Using Unstructured Grids," 36th AIAA Aerospace Sciences Meeting and Exhibit, AIAA Paper 1998-0535, Jan. 1998.

[19] Passot, T., and Pouquet, A., "Numerical Simulation of Compressible Homogeneous Flows in the Turbulent Regime," *Journal of Fluid Mechanics*, Vol. 181, No. 1, 1987, pp. 441–466. doi:10.1017/S0022112087002167

[20] Uddin, A., Kato, C., Yamade, Y., Tanahashi, M., and Miyauchi, T., "Large Eddy Simulation of Homogeneous Isotropic Turbulent Flow Using the Finite Element Method," *JSME International Journal, Series B (Fluids and Thermal Engineering)*, Vol. 49, No. 1, 2006, pp. 102–114. doi:10.1299/jsmeb.49.102

[21] Spyropoulos, E. T., and Blaisdell, G. A., "Evaluation of the Dynamic Subgrid-Scale Model for Large Eddy Simulations of Compressible Turbulent Flows," 33rd Aerospace Sciences Meeting and Exhibit, AIAA Paper 1995-355, Jan. 1995.

[22] Jimenez, J., and Wray, A. A., "The Structure of Intense Vorticity in Isotropic Turbulence," *Journal of Fluid Mechanics*, Vol. 255, No. 1, 1993, pp. 65–90. doi:10.1017/S0022112093002393

[23] Hickel, S., Adams, N. A., and Domaradzki, J. A., "An Adaptive Local Deconvolution Method for Implicit LES," *Journal of Computational Physics*, Vol. 213, No. 1, 2006, pp. 413–436. doi:10.1016/j.jcp.2005.08.017

[24] Comte-Bellot, G., and Corrsin, S., "Simple Eulerian Time Correlations of Full and Narrow Band Velocity Signals in Grid Generated Isotropic Turbulence," *Journal of Fluid Mechanics*, Vol. 48, July 1971, pp. 273–337. doi:10.1017/S0022112071001599

[25] Erlebacher, G., Hussaini, M. Y., Speziale, C. G., and Zang, T. A., "Toward the Large-Eddy Simulation of Compressible Turbulent Flows," *Journal of Fluid Mechanics*, Vol. 238, No. -1, 1992, pp. 155–185. doi:10.1017/S0022112092001678

[26] McMillan, O. J., and Ferzinger, J. H., "Direct Testing of Subgrid-Scale Models," *AIAA Journal*, Vol. 17, No. 12, 1979, pp. 1340–1346. doi:10.2514/3.61313

[27] Garnier, E., Mossi, M., and Sagaut, P., "On the Use of Shock-Capturing Schemes for Large Eddy Simulation," *Journal of Computational Physics*, Vol. 153, No. 2, 1999, pp. 273–311. doi:10.1006/jcph.1999.6268

[28] Yarusevych, S., "Investigation of Airfoil Boundary Layer Turbulent Wake Development at Low Reynolds Numbers," Ph.D. Dissertation, Univ. of Toronto, Toronto, 2006.

[29] Yarusevych, S., Sullivan, P. E., and Kawall, J. G., "Coherent Structures in an Airfoil Boundary Layer and Wake at Low Reynolds Numbers," *Physics of Fluids*, Vol. 18, No. 4, 2006, Paper 044101.

[30] Piomelli, U., and Chasnov, J. R., "Large-Eddy Simulation: Theory and Application in Transition and Turbulence Modeling," Kluwer Academic, Dordrecht, The Netherlands, 1996, pp. 269–336.

[31] Roberts, S. K., and Yaras, M. I., "Large-Eddy Simulation of Transition in a Separation Bubble," *Journal of Fluids Engineering*, Vol. 128, No. 2, 2006, pp. 232–238.